A Hierarchical Energy Balance Control Method for M^3C Based on Injecting Output Frequency Circulating Currents

Jiankai Ma, Mohamed S. A. Dahidah, *Senior Member, IEEE*, Volker Pickert, *Member, IEEE*, and James Yu

***Abstract*—This paper presents a simplified hierarchical energy balance control method for a modular multilevel matrix converter (M^3C) operating as a frequency changer (50–50/3 Hz) for low-frequency ac transmission system. The proposed method employs an independent energy balance control for each subconverter of the M^3C with only injecting the output frequency circulating current, aiming at balancing the energy among the three arms of the subconverter. Then, the modulation technique is redesigned to balance the energy among *n* submodules within each arm. The proposed method simplifies the computational complexity of the M^3C by considering the subconverter independently, enabling an easy and efficient way to control the M^3C. The feasibility of the proposed method is evaluated with normal and dynamic operation, which includes step changes in the output frequency and voltage. The performance and effectiveness of the proposed control strategy is demonstrated by extensive simulation studies and experimentally validated using a scaled-down laboratory prototype.**

***Index Terms*—Circulating currents control, independent subconverter control, low-frequency ac (LFac) transmission system, modular multilevel matrix converter (M^3C).**

I. Introduction

THE ever growing demand for renewable energy due to environmental and economic concerns has resulted in huge investments in wind energy in general and large offshore wind farms in particular. The low-frequency ac (LFac) transmission system has shown promising benefits for transmitting offshore energy over medium distances (30–150 km) when compared with high-voltage dc (HVdc) and high-voltage ac (HVac) system [1]. LFAC was first proposed as a fractional frequency transmission system in [2] and then its feasibility was evaluated by interconnecting two frequency systems for hydropower plant [3]. In [4], the preliminary experiments further indicated that the transmission capacity of LFac increases by 2.5 × when compared with HVac. Furthermore, Tang *et al.* [5] presented a thorough comparison between HVdc and LFac systems. While HVdc shows a favorable performance over a long distance compared to other transmission systems, however, the lack of reliable dc/dc circuit breakers has imposed challenging constraints on such a system when realizing a multiterminal network. A case study in [6] elaborated that the LFac has a promising potential for practical implementation within an offshore wind farm. Thereby, the LFac is chosen for the offshore wind farm.

The backbone of LFac is the power converter, which works as a frequency changer. Different converters have been considered and discussed in the literature and the six-pulse cycloconverter was attempted to triple the frequency in LFac, from 50/3 to 50 Hz in [4]. Experimental results confirmed its usability but the high total harmonic distortion (THD) makes it inefficient. A different variation was then presented in [7], where the 6-pulse cycloconverter is replaced by a 12-pulse cycloconverter aiming to reduce the THD. However, as confirmed by Chen *et al.* [8], the 12-pulse cycloconverter still requires large filters to suppress the lower order harmonics. Therefore, back-to-back ac–dc–ac converters are considered as an alternative by researchers instead of the conventional ac–ac converter [5]. The modular multilevel converter (MMC) is a mature technology in voltage source converter (VSC)-HVdc, which apparently the back-to-back arrangement is a good candidate for the LFac system. Debnath *et al.* [9] highlighted that the modular design of an MMC provides the capability of meeting any voltage level requirements. Meanwhile, compared with the cycloconverter, it has a superior harmonic performance [10]. However, as discussed in [4], the structure of the half-bridge submodule (SM) in MMC does not allow to clear the dc bus short-circuit fault, which is a major limitation.

The modular multilevel matrix converter (M^3C) is recognized as the next-generation ac–ac converter for LFac. The concept and operation of the M^3C was first introduced in [11]. Later on, the space vector control was adapted to control this converter in [12]–[14]. These works also confirm the ability of the M^3C to overcome the dominated matrix converters' limitation of low-voltage conversion ratio (i.e., $V_{\text{out}}/V_{\text{in}} = 0.866$). A new structure of the M^3C with arm inductors was later proposed in [15], where each of the nine converter arms functions as a current source, aiming at overcoming the short-circuit problem. This structure utilizes the feedforward control method and the simulation results showed its steady-state operation. Furthermore, Oates and Mondal [16] introduced nine circulating current paths

Manuscript received February 27, 2019; revised June 2, 2019; accepted July 17, 2019. Date of publication July 24, 2019; date of current version December 13, 2019. This work was supported by SP Energy Networks through the Network Innovation Allowance Project No. RES/0560/7466/002. Recommended for publication by Associate Editor G. Oriti. *(Corresponding author: Jiankai Ma.)*

J. Ma, M. S. A. Dahidah, and V. Pickert are with Newcastle University, Newcastle Upon Tyne NE1 7RU, U.K. (e-mail: j.ma13@newcastle.ac.uk; mohamed.dahidah@newcastle.ac.uk; volker.pickert@newcastle.ac.uk).

J. Yu is with the SP Energy Networks, Glasgow G32 8FA, U.K. (e-mail: james.yu@scottishpower.com).

Color versions of one or more of the figures in this paper are available online at http://ieeexplore.ieee.org.

Digital Object Identifier 10.1109/TPEL.2019.2931048

of the M^{3}C builds on the results of [15] and utilized the four of nine circulating currents to balance the capacitor voltages of the SMs. The commonly used mathematical model of the M^{3}C is based on the "double $\alpha\beta0$ transformation" control method which was proposed in [17]–[20], where the control algorithm is designed based on the sophisticated mathematical calculation which requires multiple $\alpha\beta0$ transformations to decouple the input current, output current, and circulating current. It results in a very complex analysis of the mathematical relationship between the arm power and the capacitor voltage. According to that mathematical relationship, the circulating current which contains both input and output frequency components is used to balance the capacitor voltage. Diaz *et al.* [21] applied this "double $\alpha\beta0$ transformation" control method into an MW wind energy conversion system. Liu *et al.* [22] proposed the "dq transformation" control method based on [20] where the current is transformed to *dq*-axis dc signals for a better performance. The capacitor voltage fluctuations of the M^{3}C are significant when the input/output frequency get close to each other. In order to solve this problem, Fan *et al.* [23] reallocates the arm currents by only using the inner circulating currents. However, this control method is also developed from [20]. A generalized control method for MMC topologies (MMC, M^{3}C, etc.) is proposed in [24]. It presents a current control based on the state-space representation and an optimized arm energy balancing control which has been applied to the M^{3}C as an example. It concluded that the cases presented in [20] are boundary cases of their proposed control method and their method has better performance. However, these two methods both need a very complex control algorithm and associated mathematical calculation. Nakamori *et al.* [25] proposed the method that decouples the subconverter currents into positive, negative, and zero sequences in order to control the input current, circulating current, and output current independently. It uses the negative sequence circulating current, which is running at the input frequency, to balance the interarm dc-link voltages within each subconverter. This idea is similar to the commonly used "negative sequence current injection" methods in the star-connected cascaded H-bridge converters [26]. Several predictive control methods are also developed for the M^{3}C in [27]–[30]. However, predictive control method needs accurate system parameters and a huge amount of real time calculation which makes it less practical.

The arm current contains both input and output frequency components, which makes the control of the M^{3}C challenging. In this paper, the injection of the output frequency circulating current is proposed to resolve this problem. The M^{3}C is divided into three subconverters with each subconverter being controlled independently. Three arms in each subconverter share the same output phase, where the phase angle of the corresponding output voltage is set as the reference phase angle for the circulating current to balance the capacitor voltage. Meanwhile, the selective voltage mapping modulation technique (SVMM) has been developed to balance the energy between *n* SMs within each arm. The complexity and associated mathematical calculation has been dramatically reduced compared with earlier methods proposed in the literature. Experimental results confirm the simulation results and further demonstrated a comparable performance with other relevant papers presented in the literature.

The rest of this paper is organized as follows. Section II presents the circuit topology and the mathematical model of the proposed M^{3}C. Section III discusses the proposed control strategy in detail. Section IV highlights the representative simulation results for a medium-voltage system model. The experimental validation based on a small laboratory prototype has proven the viability of the proposed simplified control method under different operating conditions as presented in Section V. Finally, this paper is concluded in Section VI.

II. Modular Multilevel Matrix Converter

A. Circuit Configuration of the Proposed M^{3}C

Fig. 1 shows the circuit diagram of the M^{3}C, which is functioning as an interface between two power systems with different frequencies. In this paper, the input of the M^{3}C is connected to the offshore wind farm (50/3 Hz), where the three-phase voltages and currents are annotated as uppercase letter: e_A and i_A, e_B and i_B, e_C and i_C, respectively. (E_A, E_B, and E_C are the rms value of the input voltages, while I_A, I_B, and I_C are the rms value of the input current). On the other hand, the output of the M^{3}C is connected to the onshore gird (50 Hz), where the three-phase output voltages and currents are annotated as lowercase letter: e_a and i_a, e_b and i_b, e_c and i_c, respectively. (E_a, E_b, and E_c are the rms value of the output voltages, while I_a, I_b, and I_c are the rms value of the input current).

The analysis of the proposed M^{3}C is based on dividing the converter into three subconverters and each subconverter consists of three arms. Each arm is numbered consecutively according to the three phases of the input and output sides. The input side of each arm is denoted as *x* (i.e., $x =$ A, B, C) according to phase A, B, and C, respectively. Similarly, the output side of each arm is denoted as *y* (i.e., $y =$ a, b, c) according to phase a, b, and c, respectively. Therefore, each arm in the M^{3}C is represented as arm$_{xy}$ and the output current of the corresponding arm is i_{xy}, while the output voltage of the corresponding arm is u_{xy}. In each arm, there are *n* SMs connected in series with an arm inductor. Each SM is constructed by a full-bridge converter cell using four insulated gate bipolar transistor (IGBT) switches with their associated antiparallel diodes and one dc capacitor. The dc capacitor is denoted by C_{xyz} (i.e., $z = 1, 2, \ldots, n$). The output voltage of each SM u_{xyz} has three different possible voltage levels, i.e., u_{xyz}, 0, and $-u_{xyz}$, determined by the states of the four IGBT switches. Consequently, the dc capacitor of each SM has three states, i.e., charging, discharging, and bypassed, according to the switching states of the IGBT switch and the direction of the arm current given in Table I.

B. Mathematical Modeling of Subconverter a

As illustrated in Fig. 1, the M^{3}C is divided into three identical subconverters. For simplicity and owing to the symmetry properties, only subconverter a is considered for deriving the mathematical model in this section. However, this can be equally applied to the other subconverters of the M^{3}C.

As injecting the output frequency circulating current, each arm current contains three current components: the input current component, the output current component, and the circulating

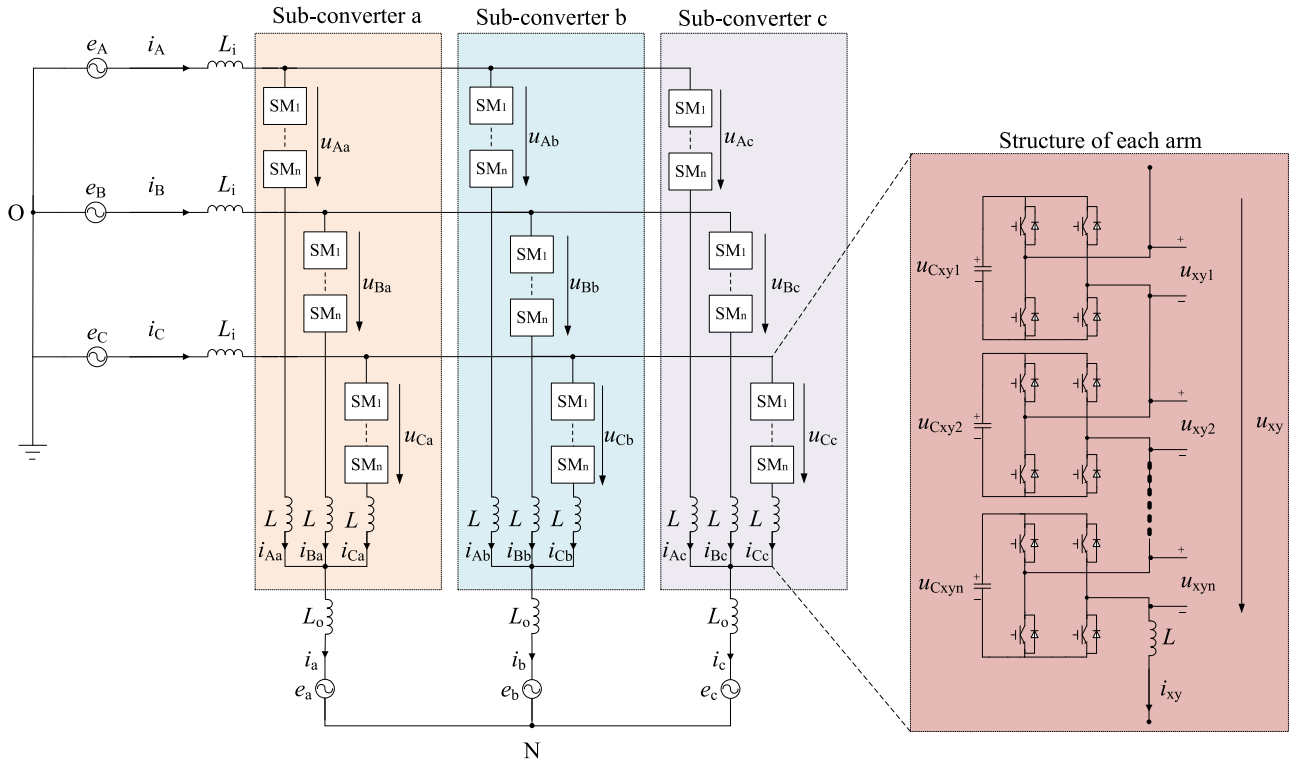

Fig. 1. Circuit diagram of the M^{3}C.

TABLE I
SWITCHING STATES OF SM

Status	S_1	S_2	S_3	S_4	i_{xy}	u_{xyz}	*Capacitor*
1	0	1	1	0	<0	-u_{Cxyz}	Charging
2	0	1	1	0	>0	-u_{Cxyz}	Discharging
3	1	0	0	1	<0	u_{Cxyz}	Discharging
4	1	0	0	1	>0	u_{Cxyz}	Charging
5	0	1	0	1	/	0	Bypassed
6	1	0	1	0	/	0	Bypassed

current component. For better presentation and discussion in the following sections, the input is represented by abbreviated letter i and the output is represented by abbreviated letter o, while the circulating current is represented by cir. Therefore, the arm current in subconverter a is given as follows:

$$\begin{cases} i_{\mathrm{Aa}} = i_{\mathrm{Aa\_i}} + i_{\mathrm{Aa\_o}} + i_{\mathrm{Aa\_cir}} \\ i_{\mathrm{Ba}} = i_{\mathrm{Ba\_i}} + i_{\mathrm{Ba\_o}} + i_{\mathrm{Ba\_cir}} \\ i_{\mathrm{Ca}} = i_{\mathrm{Ca\_i}} + i_{\mathrm{Ca\_o}} + i_{\mathrm{Ca\_cir}} \end{cases} \tag{1}$$

where $i_{\mathrm{Aa\_i}}$, $i_{\mathrm{Ba\_i}}$, and $i_{\mathrm{Ca\_i}}$ are the input current components and $i_{\mathrm{Aa\_o}}$, $i_{\mathrm{Ba\_o}}$, and $i_{\mathrm{Ca\_o}}$ are the output current components, while $i_{\mathrm{Aa\_cir}}$, $i_{\mathrm{Ba\_cir}}$, and $i_{\mathrm{Ca\_cir}}$ are the circulating currents.

It is worth noting that the circulating current flows within the subconverter and does not contribute to the input and output currents and the sum of the three circulating currents equals zero

$$i_{\mathrm{Aa\_cir}} + i_{\mathrm{Ba\_cir}} + i_{\mathrm{Ca\_cir}} = 0 \tag{2}$$

Due to the symmetry property of the proposed M^{3}C, the output current components are one-third of the output currents. Therefore, (1) can be further represented as follows:

$$\begin{cases} i_{\mathrm{Aa}} = i_{\mathrm{Aa\_i}} + \frac{i_{\mathrm{a}}}{3} + i_{\mathrm{Aa\_cir}} \\ i_{\mathrm{Ba}} = i_{\mathrm{Ba\_i}} + \frac{i_{\mathrm{a}}}{3} + i_{\mathrm{Ba\_cir}} \\ i_{\mathrm{Ca}} = i_{\mathrm{Ca\_i}} + \frac{i_{\mathrm{a}}}{3} + i_{\mathrm{Ca\_cir}}. \end{cases} \tag{3}$$

Hence, the arm voltage of subconverter a can be calculated as

$$\begin{cases} u_{\mathrm{Aa}} = e_{\mathrm{A}} - (3L_{\mathrm{i}} + L)\frac{di_{\mathrm{Aa\_i}}}{dt} - (3L_{\mathrm{o}} + L)\frac{di_{\mathrm{Aa\_o}}}{dt} \\ \qquad -L\frac{di_{\mathrm{Aa\_cir}}}{dt} - e_{\mathrm{a}} \\ u_{\mathrm{Ba}} = e_{\mathrm{B}} - (3L_{\mathrm{i}} + L)\frac{di_{\mathrm{Ba\_i}}}{dt} - (3L_{\mathrm{o}} + L)\frac{di_{\mathrm{Aa\_o}}}{dt} \\ \qquad -L\frac{di_{\mathrm{Ba\_cir}}}{dt} - e_{\mathrm{a}} \\ u_{\mathrm{Ca}} = e_{\mathrm{C}} - (3L_{\mathrm{i}} + L)\frac{di_{\mathrm{Ca\_i}}}{dt} - (3L_{\mathrm{o}} + L)\frac{di_{\mathrm{Aa\_o}}}{dt}. \\ \qquad -L\frac{di_{\mathrm{Ca\_cir}}}{dt} - e_{\mathrm{a}} \end{cases} \tag{4}$$

III. PROPOSED CONTROL STRATEGY

This section utilizes the developed mathematical model presented in Section II and discusses in detail the proposed control method for the M^{3}C. The control block diagram of the proposed control method is illustrated in Fig. 2, where it is divided into three control levels as discussed in the following sections. It is worth noting that again subconverter a is considered here for the analysis while similar analysis can be applied for the other two subconverters.

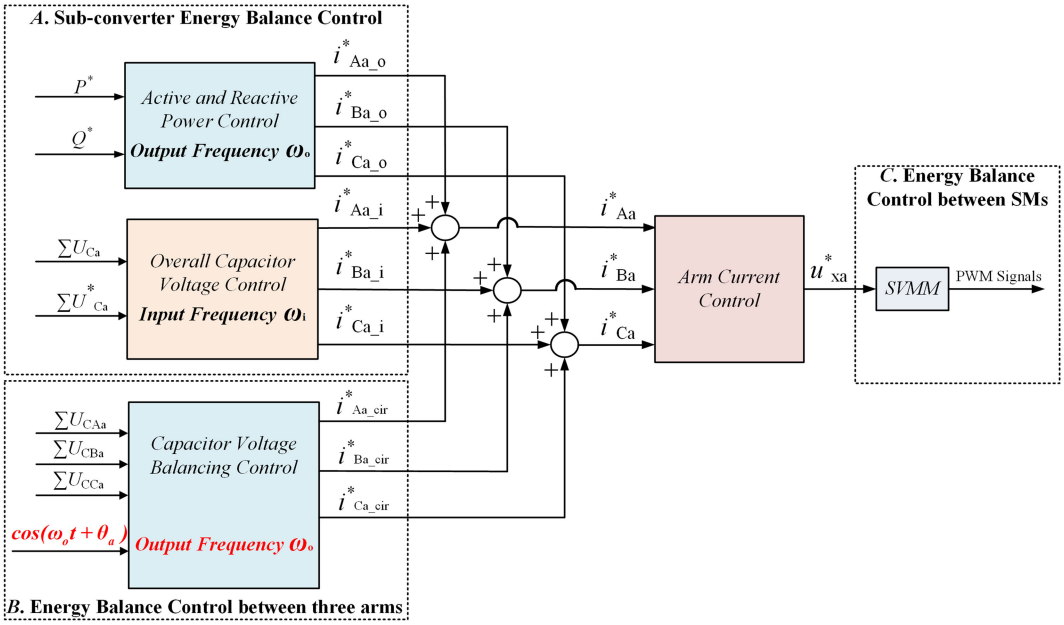

Fig. 2. Block diagram of the proposed control method in subconverter a.

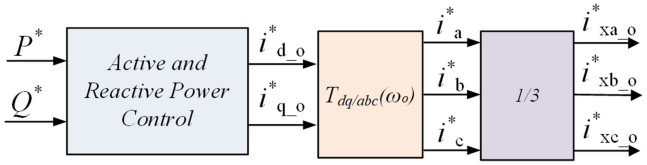

Fig. 3. Active and reactive power control block diagram.

A. Subconverter Energy Balance Control

The energy balance control of the M^{3}C requires that the sum of all the capacitor voltages within a subconverter, which is defined as $\sum u_{Cy}$, to be maintained constant.

Taking subconverter a as an example, the sum of all the capacitor voltages is Σu_{Ca}. Furthermore, the sum of the capacitor voltages of n SMs of each of the three arms in each subconverter is defined as Σu_{Cxy} ($x \in \{\mathrm{A}, \mathrm{B}, \mathrm{C}\}$, $y \in \{\mathrm{a}, \mathrm{b}, \mathrm{c}\}$). Hence, the sum of all the capacitor voltages in $\mathrm{arm}_{\mathrm{Aa}}$, $\mathrm{arm}_{\mathrm{Ba}}$, and $\mathrm{arm}_{\mathrm{Ca}}$ are Σu_{CAa}, Σu_{CBa}, and Σu_{CCa}, respectively,

$$\sum u_{\mathrm{Ca}} = \sum u_{\mathrm{CAa}} + \sum u_{\mathrm{CBa}} + \sum u_{\mathrm{CCa}} \tag{5}$$

where $\sum u_{\mathrm{CAa}}$, $\sum u_{\mathrm{CBa}}$, and $\sum u_{\mathrm{CCa}}$ are calculated as

$$\begin{cases} \sum u_{\mathrm{CAa}} = u_{\mathrm{CAa1}} + u_{\mathrm{CAa2}} + \cdots + u_{\mathrm{CAan}} \\ \sum u_{\mathrm{CBa}} = u_{\mathrm{CBa1}} + u_{\mathrm{CBa2}} + \cdots + u_{\mathrm{CBan}} \\ \sum u_{\mathrm{CCa}} = u_{\mathrm{CCa1}} + u_{\mathrm{CCa2}} + \cdots + u_{\mathrm{CCan}}. \end{cases} \tag{6}$$

The arm current consists of the input and output current components as given by (1), where any changes in these currents will influence the Σu_{Ca} and vice versa. Hence, controlling Σu_{Ca} is the key to achieve the required energy balance.

1) Active and Reactive Power Control: In Fig. 3, $P*$ and $Q*$ are reference values of the required active and reactive power, respectively, which are dependent on the demand from the output side.

The output voltages are transferred to the dq frame (i.e., e_{d} and e_{q}) using the following equation:

$$T_{\mathrm{abc/dq}} = \sqrt{\frac{2}{3}} \begin{bmatrix} \cos\theta & \cos\left(\theta - \frac{2}{3}\pi\right) & \cos\left(\theta + \frac{2}{3}\pi\right) \\ -\sin\theta & -\sin\left(\theta - \frac{2}{3}\pi\right) & -\sin\left(\theta + \frac{2}{3}\pi\right) \end{bmatrix}. \tag{7}$$

Then, the reference values, $i^*_{\mathrm{d\_o}}$ and $i^*_{\mathrm{q\_o}}$ of the output currents, can be obtained as

$$\begin{cases} P^* = e_{\mathrm{d}} \cdot i^*_{\mathrm{d\_o}} \\ Q^* = -i^*_{\mathrm{q\_o}} \cdot e_{\mathrm{d}}. \end{cases} \tag{8}$$

Therefore, the reference values of the output currents i^*_a, i^*_b, and i^*_c can then be calculated by transforming $i^*_{\mathrm{d\_o}}$ and $i^*_{\mathrm{q\_o}}$ back to the abc frame

$$T_{\mathrm{dq/abc}} = \sqrt{\frac{2}{3}} \begin{bmatrix} \cos\theta & \sin\theta \\ \cos\left(\theta - \frac{2}{3}\pi\right) & -\sin\left(\theta - \frac{2}{3}\pi\right) \\ \cos\left(\theta + \frac{2}{3}\pi\right) & -\sin\left(\theta + \frac{2}{3}\pi\right) \end{bmatrix}. \tag{9}$$

With reference to (3), in each subconverter the output current components within the arm current are equal to one-third of the output current. Therefore, the reference value of the output current components $i^*_{\mathrm{xa\_o}}$, $i^*_{\mathrm{xb\_o}}$, and $i^*_{\mathrm{xc\_o}}$ of the nine arms currents of three subconverters in the M^{3}C has been calculated as shown in Fig. 3, where

$$i^*_{\mathrm{xy\_o}} = \frac{i^*_{\mathrm{y}}}{3}. \tag{10}$$

2) Overall Capacitor Voltage Control: In Fig. 4, the low-pass filter functions as filtering out the ac fluctuation of Σu_{Ca}. After passing through the filter, the dc capacitor voltage of Σu_{Ca} is defined as ΣU_{Ca}. ΣU^*_{Ca} is the reference value of ΣU_{Ca}. When

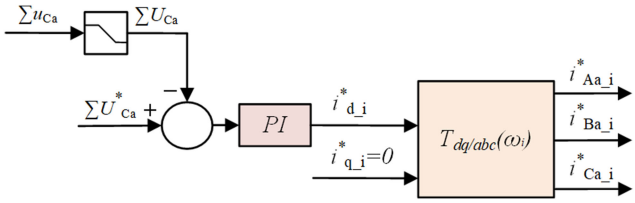

Fig. 4. Block diagram of the overall capacitor voltage control.

ΣU_{Ca} is bigger than ΣU^*_{Ca}, it means there is an extra energy that is stored within the subconverter a. Therefore, the input side must decrease the energy that is provided to this subconverter. Conversely, when ΣU_{Ca} is smaller than ΣU^*_{Ca}, it means the energy provided to the subconverter a is insufficient. Therefore, the input side must increase the energy provided to subconverter a. The ultimate goal of this control block is to keep ΣU_{Ca} equal to ΣU^*_{Ca} which means the input side meets the required energy demand.

In Fig. 4, $i^*_{\mathrm{d\_i}}$ and $i^*_{\mathrm{q\_i}}$ are the reference values of the direct- and quadrature-axis components of the input current components $i_{\mathrm{Aa\_i}}$, $i_{\mathrm{Ba\_i}}$, and $i_{\mathrm{Ca\_i}}$, respectively. Furthermore, $i^*_{\mathrm{q\_i}}$ is set to zero to achieve a unity power factor. Therefore, the reference values of the input current components $i^*_{\mathrm{Aa\_i}}$, $i^*_{\mathrm{Ba\_i}}$, and $i^*_{\mathrm{Ca\_i}}$ in Fig. 4 have been calculated according to transformation matrix (9).

It is important to mention that the amplitude of the three arm currents $i_{\mathrm{Aa\_i}}$, $i_{\mathrm{Ab\_i}}$, $i_{\mathrm{Ac\_i}}$ in subconverters a, b, c, respectively, is not necessary equaled with each other. When there is an unbalanced condition at the gird, the proposed control method is able to self-balance the energy between subconverters.

B. Energy Balance Control Between the Three Arms of the Subconverter (Capacitor Voltage Balancing Control)

Although the overall energy of the subconverter is controlled, as discussed in Section II-A, however, it is not necessarily means that the energy between the three arms of the subconverter is balanced. Therefore, another control level is required, which utilizes the circulating current. With the circulating current control, the arm with bigger energy compensates the arm with smaller energy, to realize the dynamic energy balance within each subconverter.

Fig. 5 illustrates the proposed circulating current control, which equally balances the energy across the three arms of the subconverter. The sum of all the capacitor voltages in $\mathrm{arm_{Aa}}$, $\mathrm{arm_{Ba}}$, and $\mathrm{arm_{Ca}}$ are $\sum u_{\mathrm{CAa}}$, $\sum u_{\mathrm{CBa}}$, and $\sum u_{\mathrm{CCa}}$, respectively. The low-pass filter functions as filtering out the ac fluctuation of $\sum u_{\mathrm{CAa}}$, $\sum u_{\mathrm{CBa}}$, and $\sum u_{\mathrm{CCa}}$. After passing through the filter, these three dc capacitor voltages are defined as $\sum U_{\mathrm{CAa}}$, $\sum U_{\mathrm{CBa}}$, and $\sum U_{\mathrm{CCa}}$. Then, these three values are averaged as

$$\overline{\sum U_{\mathrm{Ca}}} = \left(\sum U_{\mathrm{CAa}} + \sum U_{\mathrm{CBa}} + \sum U_{\mathrm{CCa}}\right)/3. \quad (11)$$

After $\sum U_{\mathrm{CAa}}$ and $\sum U_{\mathrm{CBa}}$ are compared with the mean value and the error is processed the PI controller, the rms value of the circulating currents $I^*_{\mathrm{Aa\_cir}}$ and $I^*_{\mathrm{Ba\_cir}}$ are then calculated as portrayed in Fig. 5.

In subconverter a, three arms are connected with output phase a, and the initial phase angle of e_a is θ_a. In order to realize the independent control of each subconverter, the frequency and initial phase angle of the respective output voltage are set as the reference phase angle of three circulating currents. Meanwhile, in order to ensure that the three circulating currents in each subconverter do not affect the respective output current, the sum of the three circulating currents is zero. The circulating current is calculated as

$$\begin{cases} i^*_{\mathrm{Aa\_cir}} = \sqrt{2} I^*_{\mathrm{Aa\_cir}} \cos(\omega_o t) \\ i^*_{\mathrm{Ba\_cir}} = \sqrt{2} I^*_{\mathrm{Ba\_cir}} \cos(\omega_o t) \\ i^*_{\mathrm{Ca\_cir}} = -i^*_{\mathrm{Aa\_cir}} - i^*_{\mathrm{Ba\_cir}}. \end{cases} \quad (12)$$

The energy difference between three arms of subconverter a is caused by the active power that is generated by the circulating currents defined by $P_{\mathrm{Aa\_cir}}$, $P_{\mathrm{Ba\_cir}}$, and $P_{\mathrm{Ca\_cir}}$ which can be calculated as follows:

$$\begin{cases} P_{\mathrm{Aa\_cir}} = i^*_{\mathrm{Aa\_cir}} \cdot u_{\mathrm{Aa}} \\ P_{\mathrm{Ba\_cir}} = i^*_{\mathrm{Ba\_cir}} \cdot u_{\mathrm{Ba}} \\ P_{\mathrm{Ca\_cir}} = i^*_{\mathrm{Ca\_cir}} \cdot u_{\mathrm{Ca}}. \end{cases} \quad (13)$$

Fig. 6 shows one possible power exchange path between the three arms in subconverter a, which is further discussed in details in the remaining of this section, when

$$\begin{cases} \sum U_{\mathrm{CAa}} - \overline{\sum U_{\mathrm{Ca}}} > 0 \\ \sum U_{\mathrm{CBa}} - \overline{\sum U_{\mathrm{Ca}}} < 0 \\ \sum U_{\mathrm{CCa}} - \overline{\sum U_{\mathrm{Ca}}} < 0. \end{cases} \quad (14)$$

After PI controller, the direction of the three circulating currents is determined as given

$$\begin{cases} I^*_{\mathrm{Aa\_cir}} > 0 \\ I^*_{\mathrm{Ba\_cir}} < 0 \\ I^*_{\mathrm{Ca\_cir}} < 0. \end{cases} \quad (15)$$

According to (13), therefore

$$\begin{cases} P_{\mathrm{Aa\_cir}} > 0 \\ P_{\mathrm{Ba\_cir}} < 0 \\ P_{\mathrm{Ca\_cir}} < 0. \end{cases} \quad (16)$$

For this condition, the $\mathrm{arm_{Aa}}$ should supply $P_{\mathrm{Aa\_cir}}$ to the output phase a, while $\mathrm{arm_{Ba}}$ and $\mathrm{arm_{Ca}}$ should absorb $P_{\mathrm{Ba\_cir}}$ and $P_{\mathrm{Ca\_cir}}$ from the output phase a. Meanwhile, when the voltage's frequency and the current's frequency are different, there is no active power generation and since the sum of the three circulating currents is equal to zero as given by (2). Therefore

$$P_{\mathrm{Aa\_cir}} + P_{\mathrm{Ba\_cir}} + P_{\mathrm{Ca\_cir}} = 0. \quad (17)$$

Therefore, $P_{\mathrm{Aa\_cir}}$, $P_{\mathrm{Ba\_cir}}$, and $P_{\mathrm{Ca\_cir}}$ only exchange between the three arms to compensate with each other in subconverter a.

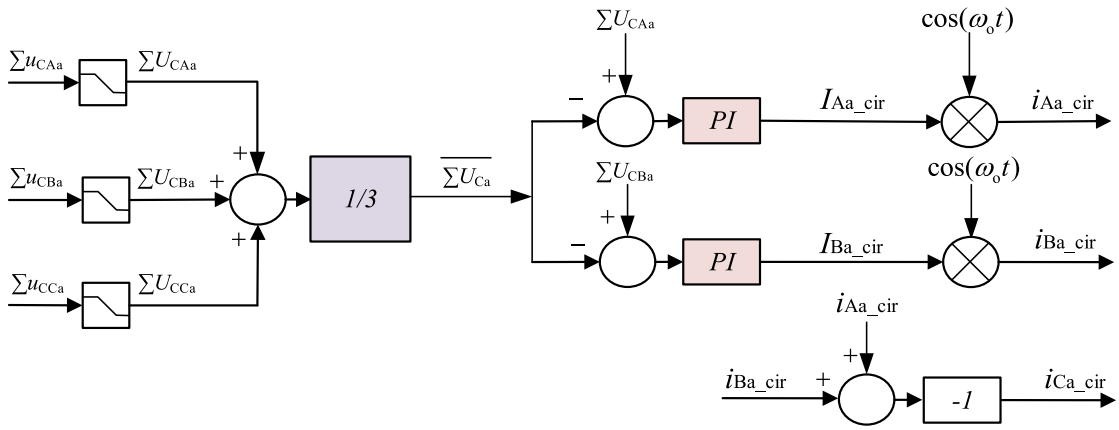

Fig. 5. Block diagram of the capacitor voltage balancing control in subconverter a.

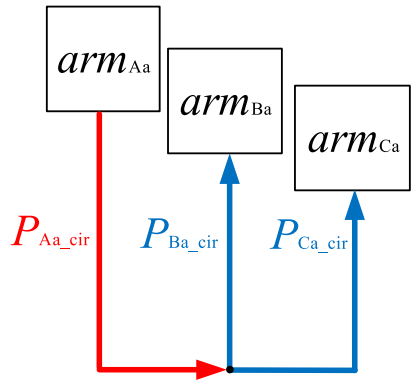

Fig. 6. One possible power exchange path.

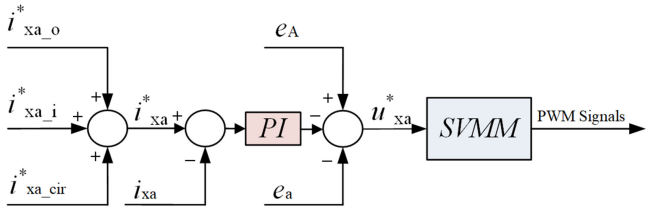

Fig. 7. Arm current control block diagram.

C. Arm Current Control

Fig. 7 shows the arm current control according to (4) in subconverter a. The reference value of the arm current i^*_{xa} consists of three current components $i^*_{\mathrm{xa\_i}}$, $i^*_{\mathrm{xa\_o}}$, and $i^*_{\mathrm{xa\_cir}}$ that have been calculated in the previous sections.

The difference between the i_{xa} and i^*_{xa} are calculated at first, after which the PI controller along with a feedforward term as per (4) is used to calculate the reference value of the three arm voltages (noted by u^*_{xa}). Then, the SVMM technique, as discussed in the following section, is designed to generate the pulsewidth modulation (PWM) signals of each SM.

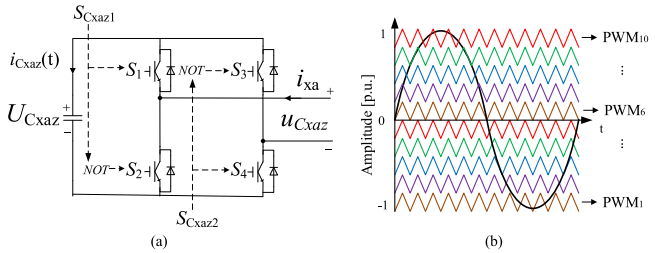

Fig. 8. (a) Full-bridge SM. (b) PWM signals of five SMs.

D. Energy Balance Control Between n SMs of Each Arm (SVMM)

In each arm, each SMs energy should be balanced which indicates the balance of the capacitor voltage. Therefore, a third control level is required to control the SMs capacitors voltage. The SVMM is designed based on the phase disposition modulation method but the sorting algorithm is specifically designed for the M^{3}C. The voltages of all SMs capacitors are being measured and sorted according to their values. Then, based on the arm current's direction these capacitors are mapped according to the sorting algorithm to realize the goal of balancing energy between the *n* SMs. The details of the control strategy are further explained below.

The instantaneous power of each SM is defined as $p_{\mathrm{C}xyz}$. The dc capacitor voltage of the SM is defined as $U_{\mathrm{C}xyz}$ as discussed in the previous section. The reference value of the dc capacitor voltage is defined as $U^*_{\mathrm{C}xyz}$. Each SM needs two switching signals which can be presented as $S_{\mathrm{C}xaz1}$ and $S_{\mathrm{C}xaz2}$ in subconverter a, as shown in Fig. 8(a). Assuming there are five SMs in arm$_{\mathrm{Aa}}$ of subconverter a, then two switching signals are $S_{\mathrm{CA}az1}$ and $S_{\mathrm{CA}az2}$. Therefore, the output voltage of the SM in arm$_{\mathrm{Aa}}$ is determined from

$$u_{\mathrm{CAaz}} = S_{\mathrm{CAaz1}} \cdot U_{\mathrm{CAaz}} - (1 - S_{\mathrm{CAaz2}}) \cdot U_{\mathrm{CAaz}} \qquad (18)$$

where as the instantaneous power of each SM is calculated as

$$p_{\mathrm{CAaz}} = u_{\mathrm{CAaz}} \cdot i_{\mathrm{Aa}} = (S_{\mathrm{CAaz1}} + S_{\mathrm{CAaz2}} - 1) \cdot U_{\mathrm{CAaz}} \cdot i_{\mathrm{Aa}}. \qquad (19)$$

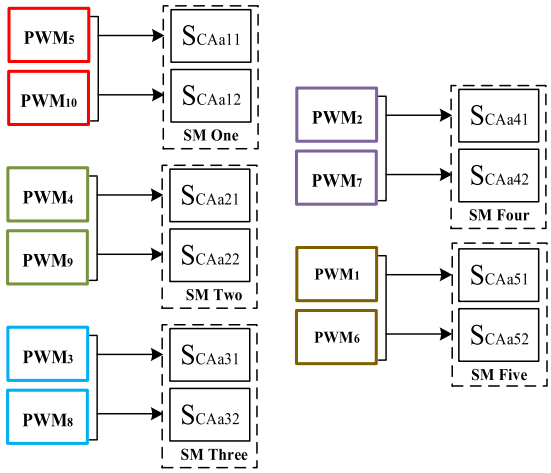

Fig. 9. PWM signals mapping of SVMM.

Hence

$$\begin{cases} p_{\mathrm{CAa1}} = u_{\mathrm{CAa1}} \cdot i_{\mathrm{Aa}} \\ \qquad = (S_{\mathrm{CAa11}} + S_{\mathrm{CAa12}} - 1) \cdot U_{\mathrm{CAa1}} \cdot i_{\mathrm{Aa}} \\ p_{\mathrm{CAa2}} = u_{\mathrm{CAa2}} \cdot i_{\mathrm{Aa}} \\ \qquad = (S_{\mathrm{CAa21}} + S_{\mathrm{CAa22}} - 1) \cdot U_{\mathrm{CAa2}} \cdot i_{\mathrm{Aa}} \\ \qquad \vdots \\ p_{\mathrm{CAa5}} = u_{\mathrm{CAa5}} \cdot i_{\mathrm{Aa}} \\ \qquad = (S_{\mathrm{CAa51}} + S_{\mathrm{CAa52}} - 1) \cdot U_{\mathrm{CAa5}} \cdot i_{\mathrm{Aa}}. \end{cases} \tag{20}$$

In Fig. 8(b), the reference value of the arm voltage u^*_{Aa} is the reference signal and there are ten carrier signals in terms of five SMs. It generates ten PWM signals that defined as PWM_1, PWM_2, …, PWM_{10}. For example, when $i_{\mathrm{Aa}} > 0$, each SMs instantaneous power could be sorted descending as

$$\begin{cases} (\mathrm{PWM}_5 + \mathrm{PWM}_{10} - 1) \cdot U^*_{Cxyz} \cdot i_{\mathrm{Aa}} \\ \quad > (\mathrm{PWM}_4 + \mathrm{PWM}_9 - 1) \cdot U^*_{Cxyz} \cdot i_{\mathrm{Aa}} \\ (\mathrm{PWM}_4 + \mathrm{PWM}_9 - 1) \cdot U^*_{Cxyz} \cdot i_{\mathrm{Aa}} \\ \quad > (\mathrm{PWM}_3 + \mathrm{PWM}_8 - 1) \cdot U^*_{Cxyz} \cdot i_{\mathrm{Aa}} \\ (\mathrm{PWM}_3 + \mathrm{PWM}_8 - 1) \cdot U^*_{Cxyz} \cdot i_{\mathrm{Aa}} \\ \quad > (\mathrm{PWM}_2 + \mathrm{PWM}_7 - 1) \cdot U^*_{Cxyz} \cdot i_{\mathrm{Aa}} \\ (\mathrm{PWM}_2 + \mathrm{PWM}_7 - 1) \cdot U^*_{Cxyz} \cdot i_{\mathrm{Aa}} \\ \quad > (\mathrm{PWM}_1 + \mathrm{PWM}_6 - 1) \cdot U^*_{Cxyz} \cdot i_{\mathrm{Aa}}. \end{cases} \tag{21}$$

Then, the capacitor voltages should be sorted ascending in order to balance the energy between five SMs in $\mathrm{arm}_{\mathrm{Aa}}$. Assuming $U_{CAa1} < U_{CAa2} < U_{CAa3} < U_{CAa4} < U_{CAa5}$, then PWM signals should be mapped to the certain switching signals of each SM, as shown in Fig. 9, which enables the balancing of the capacitors voltage within each arm.

IV. Simulation Results

The simulation model of the $\mathrm{M^3C}$ for LFac is developed using MATLAB/Simulink software. The input side of the $\mathrm{M^3C}$ is connected to the offshore wind farm (50/3 Hz), while the output side is connected with the onshore power grid (50 Hz). The simulation parameters are given in Table II. There are five capacitors in each arm. The standard 6.6 kV 1.5 kA IGBT module, such as the product from Infineon, is considered as the power switch to build the SM. The proposed system is tested under different operating conditions to validate the effectiveness and the performance of the proposed control strategy.

TABLE II
Simulation Parameters

Description	Parameters	Value
Rated Active Power	P	10 MW
Input RMS line voltage	E_{i}	11 kV
Input frequency	f_{i}	50/3 Hz
Input inductance	L_{i}	4 mH (3.4%)
Output RMS line voltage	E_{o}	11 kV
Output frequency	f_{o}	50 Hz
Output inductance	L_{o}	4 mH (3.4%)
Arm inductance	L	5 mH (4.3%)
Capacitance of SM's capacitor	C_{xyz}	5.1 mF
Rated dc capacitor voltage	U^*_{Cxyz}	5 kV
Number of SMs per arm	n	5
Switching frequency	f_{s}	5 kHz
Carrier frequency	f_c	5 kHZ

A. Case I: Steady-State Operation

Fig. 10 shows the simulation results under the steady-state operation, where (a) and (b) shows the input voltage and input current with no phase shift, demonstrating the unity power operation. The arm current contains two frequency components as illustrated in Fig. 10(c). The capacitor voltages of $\mathrm{arm}_{\mathrm{Aa}}$ in subconverter a are illustrated in Fig. 10(e), where all the five capacitor voltages are tightly balanced around 5 kV. Furthermore, Fig. 10(f) shows the sum of the capacitor voltages of all SMs in subconverter a, which are perfectly controlled around 25 kV.

B. Case II: Dynamic Output Power Operation

Fig. 11 shows the simulation results under the dynamic output power operation. Specifically, Fig. 11(a) demonstrates the case when the active power supplied by the input side increases from 10 to 11 MW at 0.5 s, where the reactive power maintains as zero for the unity power operation. It is worth noting that the capacitor voltages in Fig. 11(e) and (f) slightly decreased to compensate the active power to the gird from 0.5 s and the proposed control

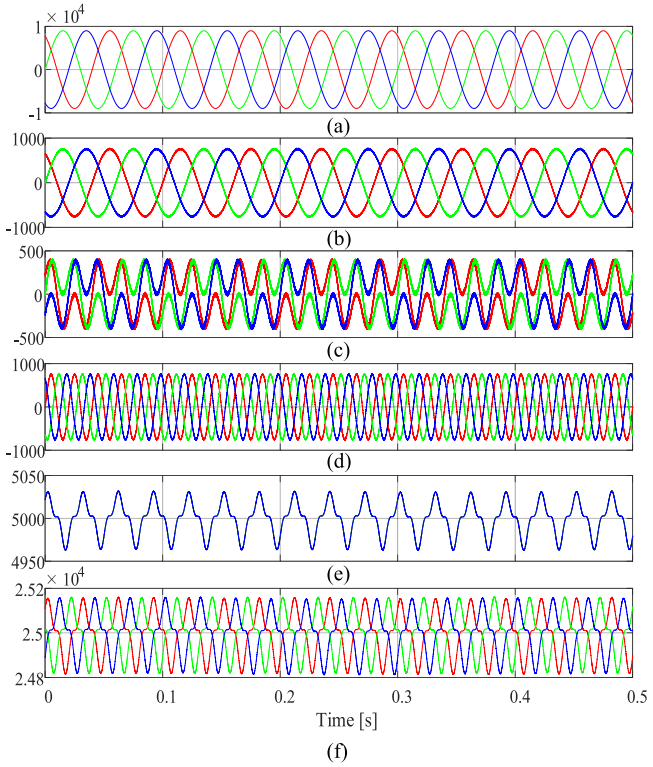

Fig. 10. Simulation results under the steady-state operation. (a) Input voltage [V]. (b) Input current [A]. (c) Arm current [A]. (d) Output current [A]. (e) Capacitor voltages [V]. (f) Sum of capacitor voltages [V].

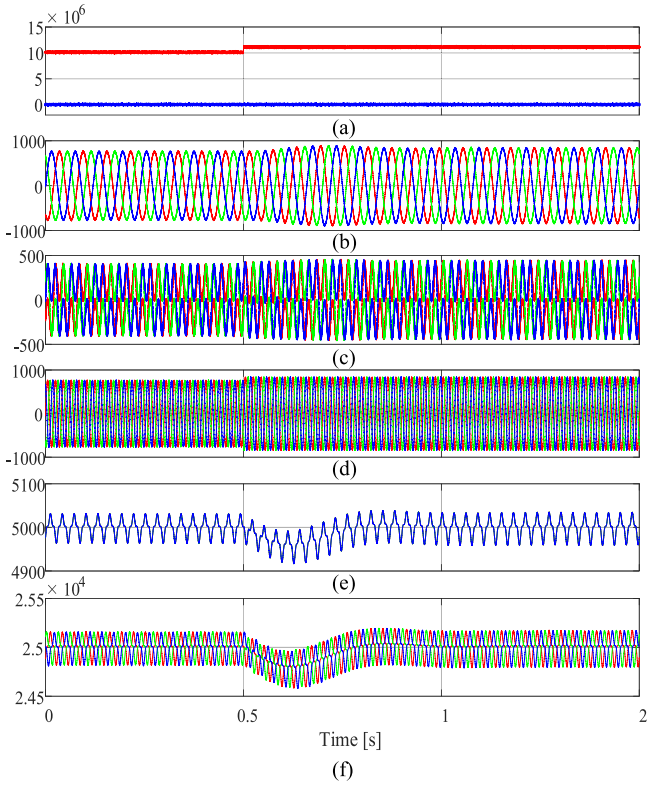

Fig. 11. Simulation results under a dynamic output power operation. (a) Active and reactive power [W]/[Var]. (b) Input current [A]. (c) Arm current [A]. (d) Output current [A]. (e) Capacitor voltages [V]. (f) Sum of capacitor voltages [V].

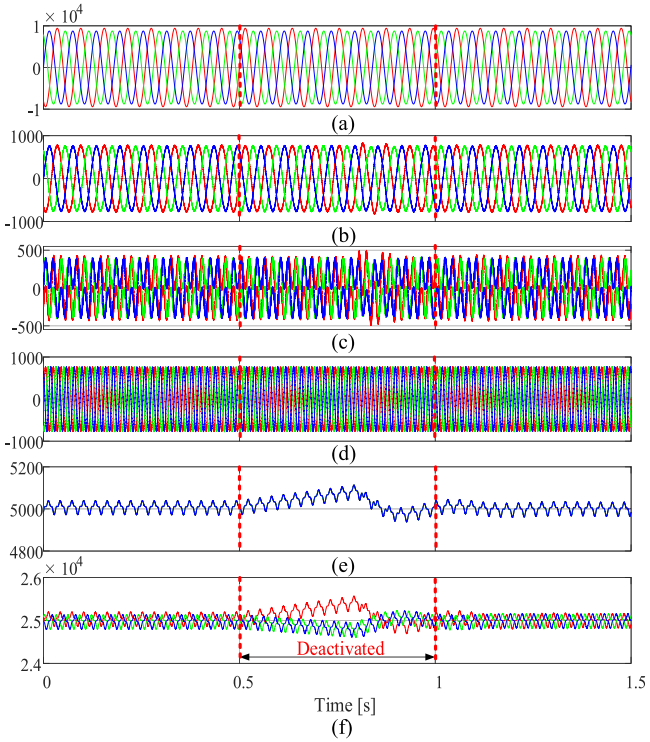

Fig. 12. Simulation results under unbalanced grid voltage condition. (a) Input voltage [V]. (b) Input current [A]. (c) Arm current [A]. (d) Output current [A]. (e) Capacitor voltages [V]. (f) Sum of capacitor voltages [V].

strategy successfully managed to maintain the voltage balance at 0.8 s.

C. Case III: Unbalanced Grid Voltage Condition

The 5% negative sequence component has been added in the input side of the M^{3}C which causes the unbalanced grid voltage condition, as shown in Fig. 12(a); the proposed control strategy illustrated the good performance under this condition. From 0.5 to 0.8 s, the capacitor voltage balancing control has been deactivated to illustrate the effect of the circulating current. As it can be noticed, from 0 to 0.5 s, the circulating current control is deactivated, which causes the five capacitors voltages in $\mathrm{arm_{Aa}}$ in subconverter a deviating (i.e., gradually increasing) from the reference voltage. This has also influenced the sum of the capacitor voltages of $\mathrm{arm_{Aa}}$ (increasing) and $\mathrm{arm_{Ba}}$, $\mathrm{arm_{Ca}}$ (decreasing), as shown in Fig. 12. On the other hand, the effect of the circulating current can be obviously observed when it is activated at 0.8 s, where the capacitor voltages are quickly rebalanced around 5 kV.

V. Experimental Results

A. Experimental Setup

Fig. 13 depicts a scaled-down laboratory prototype of the M^{3}C has been developed with the parameters tabulated in Table III to validate the effectiveness of the proposed control strategy. It should be noted that with the limited resources, the system

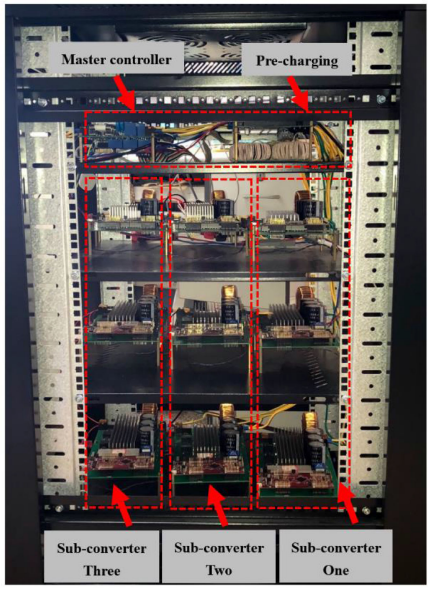

Fig. 13. Experimental setup of M^{3}C.

TABLE III
EXPERIMENTAL PARAMETERS

Description	Parameters	Value
Rated active power	P	0.63 kW
Input phase RMS voltage	E_i	60 V
Input frequency	f_i	50 Hz
Input inductance	L_i	1 mH (1.8%)
Output phase RMS voltage	E_o	56 V
Output frequency	f_o	50/3 Hz
Output inductance	L_o	1 mH (1.8%)
Capacitance of SM's capacitor	C_{xyz}	1 mF
Rated dc capacitor voltage	U^*_{Cxyz}	70 V
Arm inductance	L	4 mH (7.3%)
Load Resistance	R_o	16 Ω
Load Inductance	L_o	1 mH (1.8%)
Number of SMs per arm	n	3

demonstrated by an input voltage of 50 Hz obtained from a three-phase programmable ac source, while the output side of 50/3 Hz is connected to a three-phase inductive load. There are three subconverters within the M^{3}C. Each subconverter has three arms of which are connected in series with an arm inductor. Furthermore, there are three full-bridge SMs with a dc capacitor within each arm.

The experimental setup is realized by using a distributed control network, which consists of a total of ten controllers

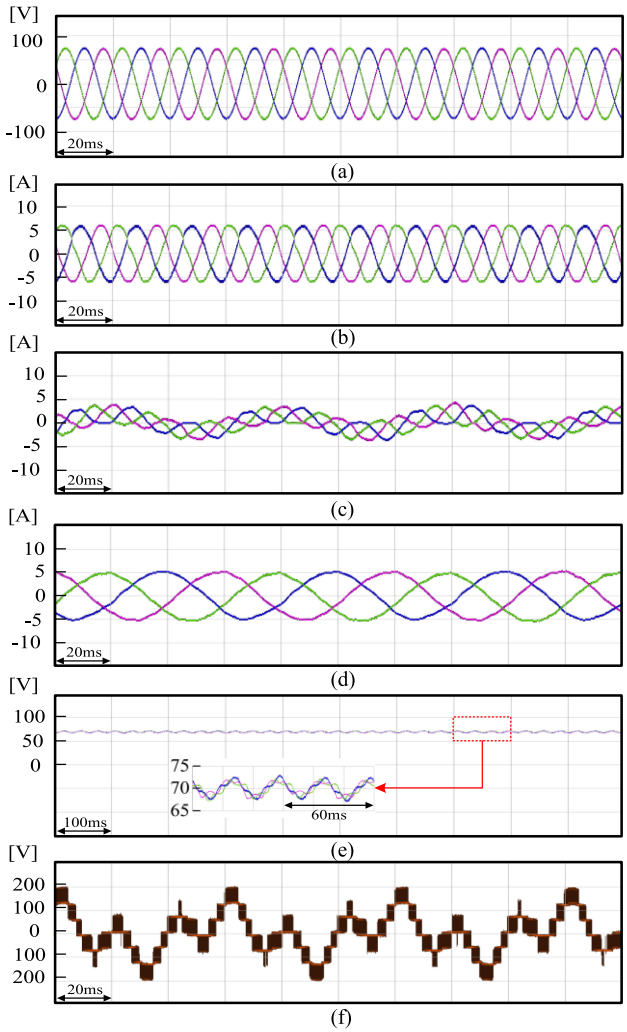

Fig. 14. Experimental results under the steady-state operation. (a) Input voltage. (b) Input current. (c) Arm current. (d) Output current. (e) Capacitor voltages. (f) Arm voltage.

(TMS320F2837xS). One master controller for the whole M^{3}C system and one controller for each arm. The communication is realized by the controller area network (CAN) system.

For completeness, the proposed system is tested experimentally under different operating conditions to verify its performance and effectiveness as discussed in the following sections.

B. Experimental Results

Fig. 14 shows the experimental results of the M^{3}C under the steady-state operation condition. Specifically, Fig. 14(b) shows the input current is in-phase with the input voltage, which demonstrates the unity power factor operation achieved by the proposed control method. The output current has been controlled well with the desired low frequency of 50/3 Hz, as can be seen from Fig. 14(d).

As expected, the arm current contains two frequency components, which are experimentally shown in Fig. 14(c). Once again, the circulating current has no effect on either the input or the output currents as demonstrated experimentally in

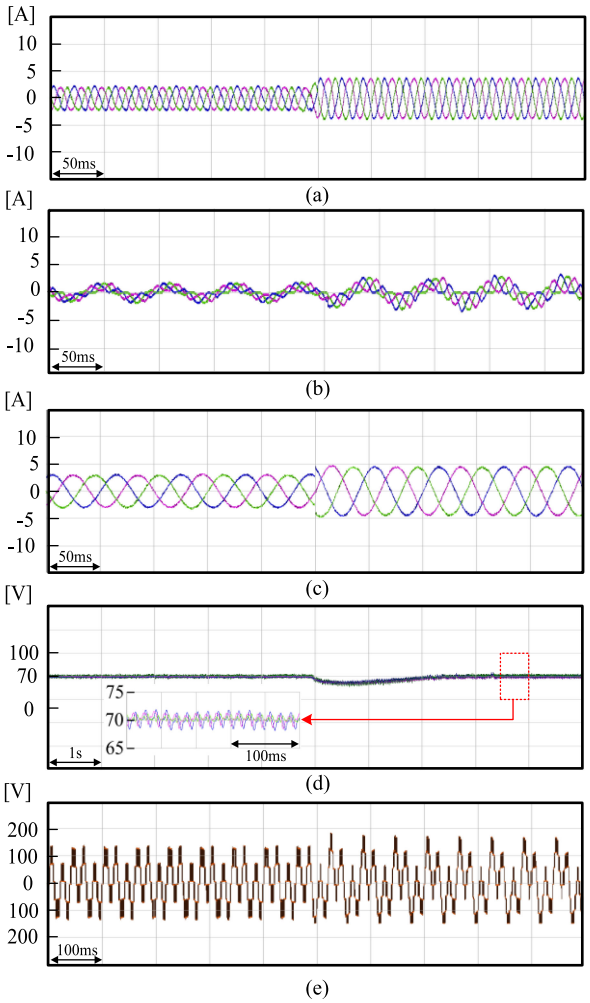

Fig. 15. Experimental results under the output voltage step change operation. (a) Input current. (b) Arm current. (c) Output current. (d) Capacitor voltages. (e) Arm voltage.

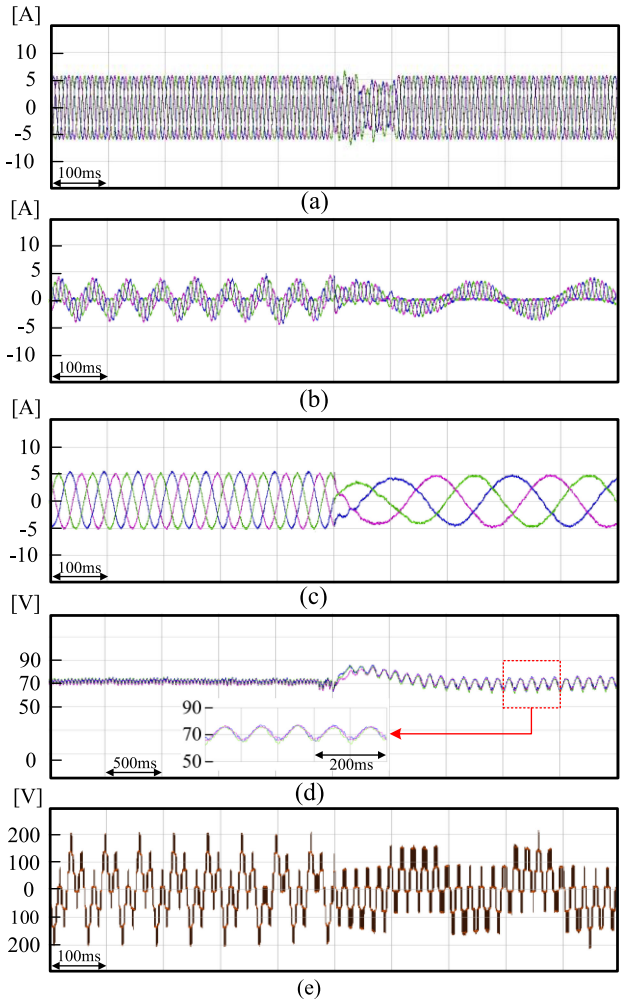

Fig. 16. Experimental results under the output frequency step change operation. (a) Input current. (b) Arm current. (c) Output current. (d) Capacitor voltages. (e) Arm voltage.

Fig. 14(b)–(d). Three capacitor voltages are presented in Fig. 14(e), where the zoomed figure shows the voltage fluctuates by only ± 2 V from the desired voltage of 70 V, which again confirms the effectiveness of the proposed control technique. Finally, the output voltage of arm_{Aa} is shown in Fig. 14(f).

Furthermore, the performance of the proposed system is experimentally validated with two step change operating conditions. Fig. 15 illustrates the step change in the output frequency, i.e., 50/3–5 Hz. The lower the output frequency, the higher the ac voltage ripple of the capacitor voltage. This test aims to demonstrate the performance of the proposed control technique with a very low output frequency. However, the measured capacitor voltages shows only ± 2 V variation from the 70 V reference voltage as shown in Fig. 15(d), which again proves the robustness of the control method.

Step change in the output voltage is also demonstrated experimentally, where the voltage changed from 43 to 56 V as portrayed in Fig. 16. As the demand on the output side increased, as shown in Fig. 16(c), the input current increases accordingly, as depicted in Fig. 16(a). Three capacitor voltages damped for compensating the increasing power demand from the output side, but well balanced at 70 V.

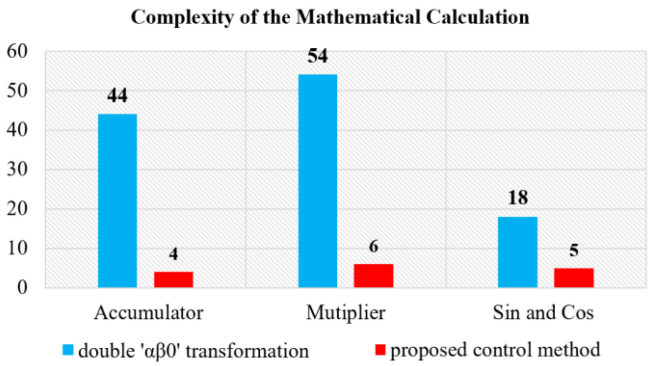

Fig. 17. Comparison between the "double $\alpha\beta 0$ transformation" and the proposed control method.

C. Comparison Between "Double $\alpha\beta 0$ Transformation" Control Method and the Proposed Control Method

In terms of the complexity of the voltage balancing control, the comparison between two control methods has been shown in Fig. 17. The complexity of the mathematical calculation is determined by how many accumulator, multiplier, and sin and cos in the coding of these three methods based on the

code composer studio (CCS) platform. Obviously, the amount of accumulator, multiplier, and sin and cos of the "double $\alpha\beta 0$ transformation" control method are much more than the proposed control method. The operation time of "double $\alpha\beta 0$ transformation" control method is 4117 CPU period and the proposed control method only take half of the time, 2553 CPU period (CPU frequency is 200 MHz). Therefore, the proposed control method effectively reduced the control complexity and the associated mathematical calculation with reduced operation time. It is important to mention that all the data are based on the coding of the author to achieve the fairest results.

VI. Conclusion

The proposed control method achieved the fully independent control of each subconverter. The injection of the output frequency circulating current has been designed easily and accurately for the purpose of compensating the energy difference between the three arms of the subconverter. The SVMM technique is designed that balances the energy between *n* SMs within each arm. The experimental results from a scaled-down laboratory prototype proved the performance of the proposed control method under steady state and different dynamic operating conditions.

References

[1] N. Qin, S. You, Z. Xu, and V. Akhmatov, "Offshore wind farm connection with low frequency AC transmission technology," in *Proc. IEEE Power Energy Soc. General Meeting*, Calgary, AB, Canada, 2009, pp. 1–8.

[2] X. Wang, "The fractional frequency transmission system," in *Proc. Inst. Elect. Eng. Japan Power Energy*, Tokyo, Japan, Jul. 1994, pp. 53–58.

[3] X. Wang and X. Wang, "Feasibility study of fractional frequency transmission system," *IEEE Trans. Power Syst.*, vol. 11, no. 2, pp. 962–967, May 1996.

[4] W. Xifan, C. Chengjun, and Z. Zhichao, "Experiment on fractional frequency transmission system," *IEEE Trans. Power Syst.*, vol. 21, no. 1, pp. 372–377, Feb. 2006.

[5] Y. Tang, P. B. Wyllie, J. Yu, X. M. Wang, L. Ran, and O. Alatise, "Offshore low frequency AC transmission with back-to-back modular multilevel converter (MMC)," in *Proc. 11th IET Int. Conf. AC DC Power Trans.*, Birmingham, U.K., 2015, pp. 1–8.

[6] W. Xifan, T. Yufei, N. Lianhui, M. Yongqing, and X. Zhao, "Feasibility of integrating large wind farm via fractional frequency transmission system a case study," *Int. Trans. Elect. Energy Syst.*, vol. 24, pp. 64–74, Jan. 2013.

[7] N. Lianhui, W. Xifan, and T. Yufei, "Experiment on wind power integration grid via fractional frequency transmission system: Realization of the variable-speed variable-frequency power wind," in *Proc. 4th Int. Conf. Elect. Utility Deregulation Restructuring Power Technol.*, Weihai, China, 2011, pp. 444–449.

[8] H. Chen, M. H. Johnson, and D. C. Aliprantis, "Low-frequency AC transmission for offshore wind power," *IEEE Trans. Power Del.*, vol. 28, no. 4, pp. 2236–2244, Oct. 2013.

[9] S. Debnath, J. Qin, B. Bahrani, M. Saeedifard, and P. Barbosa, "Operation, control, and applications of the modular multilevel converter: A review," *IEEE Trans. Power Electron.*, vol. 30, no. 1, pp. 37–53, Jan. 2015.

[10] M. A. Perez, S. Bernet, J. Rodriguez, S. Kouro, and R. Lizana, "Circuit topologies, modeling, control schemes, and applications of modular multilevel converters," *IEEE Trans. Power Electron.*, vol. 30, no. 1, pp. 4–17, Jan. 2015.

[11] R. W. Erickson and O. A. Al-Naseem, "A new family of matrix converters," in *Proc. 27th Annu. Conf. IEEE Ind. Electron. Soc.*, Denver, CO, USA, 2001, vol. 2, pp. 1515–1520.

[12] S. Angkititrakul and R. W. Erickson, "Control and implementation of a new modular matrix converter," in *Proc. 19th Annu. IEEE Appl. Power Electron. Conf. Expo.*, 2004, vol. 2, pp. 813–819.

[13] Y. Miura, T. Mizutani, M. Ito, and T. Ise, "A novel space vector control with capacitor voltage balancing for a multilevel modular matrix converter," in *Proc. IEEE ECCE Asia Downunder*, Melbourne, VIC, Australia, 2013, pp. 442–448.

[14] S. Angkititrakul and R. W. Erickson, "Capacitor voltage balancing control for a modular matrix converter," in *Proc. 21st Annu. IEEE Appl. Power Electron. Conf. Expo.*, Dallas, TX, USA, 2006, pp. 1659–1665.

[15] C. Oates, "A methodology for developing 'Chainlink' converters," in *Proc. 13th Eur. Conf. Power Electron. Appl.*, Barcelona, Spain, 2009, pp. 1–10.

[16] C. Oates and G. Mondal, "DC circulating current for capacitor voltage balancing in modular multilevel matrix converter," in *Proc. 14th Eur. Conf. Power Electron. Appl.*, Birmingham, U.K., 2011, pp. 1–7.

[17] F. Kammerer, J. Kolb, and M. Braun, "A novel cascaded vector control scheme for the modular multilevel matrix converter," in *Proc. 37th Annu. Conf. IEEE Ind. Electron. Soc.*, Melbourne, VIC, Australia, 2011, pp. 1097–1102.

[18] F. Kammerer, M. Gommeringer, J. Kolb, and M. Braun, "Energy balancing of the modular multilevel matrix converter based on a new transformed arm power analysis," in *Proc. 16th Eur. Conf. Power Electron. Appl.*, Lappeenranta, Finland, 2014, pp. 1–10.

[19] F. Kammerer, J. Kolb, and M. Braun, "Fully decoupled current control and energy balancing of the modular multilevel matrix converter," in *Proc. 15th Int. Power Electron. Motion Control Conf.*, Novi Sad, Serbia, 2012, Paper LS2a.3.

[20] W. Kawamura, M. Hagiwara, and H. Akagi, "Control and experiment of a modular multilevel cascade converter based on triple-star bridge cells," *IEEE Trans. Ind. Appl.*, vol. 50, no. 5, pp. 3536–3548, Sep./Oct. 2014.

[21] M. Diaz *et al.*, "Control of wind energy conversion systems based on the modular multilevel matrix converter," *IEEE Trans. Ind. Electron.*, vol. 64, no. 11, pp. 8799–8810, Nov. 2017.

[22] S. Liu, X. Wang, Y. Meng, P. Sun, H. Luo, and B. Wang, "A decoupled control strategy of modular multilevel matrix converter for fractional frequency transmission system," *IEEE Trans. Power Del.*, vol. 32, no. 4, pp. 2111–2121, Aug. 2017.

[23] B. Fan, K. Wang, P. Wheeler, C. Gu, and Y. Li, "A branch current reallocation based energy balancing strategy for the modular multilevel matrix converter operating around equal frequency," *IEEE Trans. Power Electron.*, vol. 33, no. 2, pp. 1105–1117, Feb. 2018.

[24] D. Karwatzki and A. Mertens, "Generalized control approach for a class of modular multilevel converter topologies," *IEEE Trans. Power Electron.*, vol. 33, no. 4, pp. 2888–2900, Apr. 2018.

[25] T. Nakamori, M. A. Sayed, Y. Hayashi, T. Takeshita, S. Hamada, and K. Hirao, "Independent control of input current, output voltage, and capacitor voltage balancing for a modular matrix converter," *IEEE Trans. Ind. Appl.*, vol. 51, no. 6, pp. 4623–4633, Nov./Dec. 2015.

[26] D. Lu, S. Wang, J. Yao, T. Yang, and H. Hu, "Cluster voltage regulation strategy to eliminate negative sequence currents under unbalanced grid for star-connected cascaded H-bridge STATCOM," *IEEE Trans. Power Electron.*, vol. 34, no. 3, pp. 2193–2205, Mar. 2019.

[27] A. Mora, M. Espinoza, M. Díaz, and R. Cárdenas, "Model predictive control of modular multilevel matrix converter," in *Proc. IEEE 24th Int. Symp. Ind. Electron.*, Buzios, Brazil, 2015, pp. 1074–1079.

[28] L. Huang, X. Yang, B. Zhang, L. Qiao, H. Li, and M. Tian, "Hierarchical model predictive control of modular multilevel matrix converter for low frequency AC transmission," in *Proc. 9th Int. Conf. Power Electron. ECCE Asia*, Seoul, South Korea, 2015, pp. 927–933.

[29] H. Nademi, L. E. Norum, Z. Soghomonian, and T. Undeland, "Low frequency operation of modular multilevel matrix converter using optimization-oriented predictive control scheme," in *Proc. IEEE 17th Workshop Control Model. Power Electron.*, Trondheim, Norway, 2016, pp. 1–6.

[30] B. Fan, K. Wang, P. Wheeler, C. Gu, and Y. Li, "An optimal full frequency control strategy for the modular multilevel matrix converter based on predictive control," *IEEE Trans. Power Electron.*, vol. 33, no. 8, pp. 6608–6621, Aug. 2018.

Jiankai Ma was born in Jiangsu, China, in 1991. He received the B.S. degree in electrical and electronic engineering from Northumbria Unviersity, Newcastle upon Tyne, U.K., in 2014, and the Ph.D. degree in power electronics from Newcastle University, Newcastle upon Tyne, U.K., in 2019.

His research interest includes modular multilevel cascaded converters.

Mohamed S. A. Dahidah (M'02–SM'10) received the Ph.D. degree in electrical engineering from Multimedia University, Cyberjaya, Malaysia, in 2008.

He was an Assistant Professor with the Department of Electrical and Electronic Engineering, The University of Nottingham Malaysia, Semenyih, Malaysia, till November 2012. He is currently a Senior Lecturer with the School of Engineering, Newcastle University, Newcastle Upon Tyne, U.K. He has authored or coauthored a number of refereed journal and conference papers. His research interests include modular multilevel converters, SHE-PWM modulation technique for power electronics converters, battery charger for EVs, solid state transformers, and renewable energy integration.

Dr. Dahidah is the Deputy Editor-in-Chief for *IET Power Electronics* and has been a regular Reviewer for both the IEEE and IET journals.

Volker Pickert (M'04) received the Dipl.Ing. degree in electrical and electronic engineering from RWTH Aachen, Aachen, Germany, in 1994, and the Ph.D. degree in power electronics from Newcastle University, Newcastle upon Tyne, U.K., in 1997. He studied at the RWTH Aachen, and Cambridge University, Cambridge, U.K.

From 1998 to 1999, he was an Application Engineer with Semikron GmbH, Nuremberg, Germany, and from 1999 to 2003, he was a Group Leader at Volkswagen AG, Wolfsburg, Germany, responsible for the development of electric drives for electric vehicles. In 2003, he was a Senior Lecturer with Electrical Power Group, Newcastle University, and in 2011, he became a Full Professor of Power Electronics. In 2012, he became the Head of the Electrical Power Group. He has authored or coauthored more than 150 book chapters, journals, and conference papers in the area of power electronics and electric drives. His current research interests include power electronics for transport applications, thermal management, health monitoring techniques, and advanced nonlinear control.

Dr. Pickert is the active Editor-in-Chief of the *IET Power Electronics* journal. He is regularly invited as Keynote Speaker and advises various governments on energy and transport related issues. In 2019, he also became the Director of U.K.'s EPSRC Doctoral Training Centre in power electronics for sustainable electric propulsion. He was the recipient of the IMarEST Denny Medal for the Best Article in the *Journal of Marine Engineering* in 2011, and in 2018, he was the recipient of the Best Paper Award at the IEEE International Conference on Computing Electronics and Communications Engineering, Essex, U.K.

James Yu received the B.Eng. (Hons., distinction) degree in electrical and electronic engineering from Harbin Institute of Technology, China, in 1998, the M.Sc. (distinction) degree in electrical power from Newcastle University, Newcastle upon Tyne, U.K., in 2000, and the Ph.D. degree in control of doubly-fed machines from Northumbria University, Newcastle upon Tyne, U.K., in 2004.

He is a Chartered Engineer, an elected Institute of Engineering and Technology Fellow, and a Royal Engineering Academy Visiting Professor. He is the Convenor of a joint CIGRE medium voltage dc working group: C6/B4.37. He is also the Deputy U.K. Regular Member of B4 (HVdc) under CIGRE. He is currently accountable for the innovation projects delivery with SP Energy Networks, Glasgow, U.K. He joined the U.K. electricity transmission/distribution industry after he finished his studies from Newcastle upon Tyne. He has taken various technical, commercial, and managerial roles in the industry. His team are working on flagship innovation projects at national and European level, and pushing the innovation into business. He is passionate about education and fully aware of its profound impact on young people's future. He has strong commitment to the engineering higher education in the U.K. He is a Ph.D. Supervisor and Visiting Professor at various institutes, including Glasgow University, University of Newcastle upon Tyne, and the University of Manchester. He has authored or coauthored more than 50 academic papers covering electricity market, transmission network control, renewable generation, and engineering education.

Dr. Yu was the recipient of the Utilities Innovation Star Award in 2016. His team has also contributed to Utilities Smart Cities Award (2019) and the Best Utilities Award (2019).